

Accepted Manuscript

Defect formation and optical activation of Tb implanted Al_xGa_{1-x}N films using channeled implantation at different temperatures

M. Fialho, S. Magalhães, J. Rodrigues, M.P. Chauvat, P. Ruterana, T. Monteiro, K. Lorenz, E. Alves



PII: S0257-8972(18)30111-7
DOI: <https://doi.org/10.1016/j.surfcoat.2018.02.008>
Reference: SCT 23079

To appear in: *Surface & Coatings Technology*

Received date: 29 October 2017
Revised date: 1 February 2018
Accepted date: 2 February 2018

Please cite this article as: M. Fialho, S. Magalhães, J. Rodrigues, M.P. Chauvat, P. Ruterana, T. Monteiro, K. Lorenz, E. Alves, Defect formation and optical activation of Tb implanted Al_xGa_{1-x}N films using channeled implantation at different temperatures. The address for the corresponding author was captured as affiliation for all authors. Please check if appropriate. Sct(2017), <https://doi.org/10.1016/j.surfcoat.2018.02.008>

This is a PDF file of an unedited manuscript that has been accepted for publication. As a service to our customers we are providing this early version of the manuscript. The manuscript will undergo copyediting, typesetting, and review of the resulting proof before it is published in its final form. Please note that during the production process errors may be discovered which could affect the content, and all legal disclaimers that apply to the journal pertain.

Defect formation and optical activation of Tb implanted $\text{Al}_x\text{Ga}_{1-x}\text{N}$ films using channeled implantation at different temperatures

M. Fialho¹, S. Magalhães¹, J. Rodrigues², M. P. Chauvat³, P. Ruterana³, T. Monteiro², K. Lorenz¹, E. Alves¹

¹IPFN, Campus Tecnológico e Nuclear, Instituto Superior Técnico, Universidade de Lisboa, Estrada Nacional 10, 2695-066 Bobadela LRS, Portugal

²Departamento de Física e I3N, Universidade de Aveiro, 3810-193 Aveiro, Portugal

³CIMAP, UMR 6252, CNRS-ENSICAEN-CEA-UCBN, 6, Bd Marechal Juin, 14050 Caen, France

Abstract

$\text{Al}_x\text{Ga}_{1-x}\text{N}$ ($x=0.20, 0.50, 0.63$) films grown on (0001) sapphire substrates by metal organic chemical vapor phase deposition were implanted with Tb ions at 150 keV and a fluence of $7 \times 10^{14} \text{ Tb.cm}^{-2}$. The implantation was carried out with the beam aligned with the c -axis and the implantation temperature was varied from room temperature (RT) to 550 °C. Additionally, post-implantation rapid thermal annealing was performed at 1200 °C during 120 s. The impact of implantation temperature on the damage accumulation is investigated. Rutherford backscattering spectrometry/channeling (RBS/C) measurements show that two damage regions are forming and the damage is not decreasing monotonically with the increase of implantation temperature. Bulk damage follows the same trend for all $\text{Al}_x\text{Ga}_{1-x}\text{N}$ compositions, increasing when the temperature is raised up to ~100 °C, and then decreasing for higher temperatures. A good agreement is observed between the damage accumulation obtained from RBS/C and the strain profile derived from symmetric (0002) 2θ - ω X-ray diffraction scans. Transmission electron microscopy results show the suppression of basal

stacking faults after implantation at 550 °C. Tb lattice site location studies revealed two preferential sites: the substitutional cation site and a site displaced from that by 0.2 Å along the *c*-axis. A higher substitutional fraction of Tb ions is obtained for implantation temperature of 550 °C. The optical activity investigated by photoluminescence showed that after thermal annealing, the $^5D_4 \rightarrow ^7F_J$ intra-4f⁸ transition is detected in all the samples.

Keywords: Rutherford backscattering spectrometry/channeling; X-ray diffraction; Transmission electron microscopy; Photoluminescence; AlGaIn.

1. Introduction

III-nitride based semiconductors proved to have important properties suitable for optoelectronic applications [1–3]. The incorporation of rare earth (RE) ions into III-nitride compounds broadens their field of applications for full-color displays or optical communications [4–6]. Doping using ion implantation offers concentration control of implanted ions, lateral patterning and reproducibility, widening the possibilities for device design [7]. However, the defects generated during this process are detrimental for device performance and materials' properties. For III-nitride semiconductors, such as GaN, AlN and their alloys, implantation damage build-up processes are very complex and, in particular for the ternaries, poorly understood [8–12]. The mechanism of damage formation due to ion implantation in GaN and AlN showed some relevant differences between the two compounds. In particular, preferential surface damage, typical for GaN, was attributed to the mobility of point defects allowed by the dense network of basal and prismatic stacking faults resultant from ion implantation [13]. Much lower surface damage

in AlN was explained by the higher formation energy of prismatic stacking faults and therefore less efficient defect migration towards the surface than in GaN [13]. The behavior of surface damage build-up for the ternary $\text{Al}_x\text{Ga}_{1-x}\text{N}$ was shown to be similar to GaN for low AlN contents ($x=0.15$) and similar to AlN for high AlN molar fraction ($x=0.77$) [14]. Concerning damage close to the end of range, studies performed for $\text{Al}_x\text{Ga}_{1-x}\text{N}$ ($0 \leq x \leq 0.6$) indicate the increase of dynamic annealing processes and enhanced radiation resistance during heavy ion implantation on samples with higher AlN content [15]. However, for light ion implantation, a higher concentration of damage in $\text{Al}_x\text{Ga}_{1-x}\text{N}$ with higher AlN content at high fluence regime was obtained [11,12].

Post-implantation annealing treatment is required for optical activation of implanted RE ions but only partial lattice recovery is achieved even for annealing well above the growth temperature [16,17]. Additional procedures to mitigate the ion implantation effects are therefore important. Previous reports showed that performing the implantation along a major crystallographic direction reduces the lattice damage during the implantation process, as the ions are channeled along the atomic rows, reducing the number of nuclear collisions [14,18–23]. An additional way to reduce the damage could be to increase the substrate temperature during the ion implantation process, increasing the mobility of point defects, and thus promoting their recombination. In the literature, the studies performed for GaN showed some discrepancies. For instance, Parikh *et al.* [24] and Jiang *et al.* [25] reported a decreasing damage accumulation with increasing implantation temperature from room temperature (RT) to 550 °C. For the wider range investigated by Usov *et al.* the opposite tendency was found for the temperature range from 500 °C to 700 °C, with a subsequent decrease for temperatures up to 1000 °C [26]. The increase of damage between 500 °C and 700 °C was referred to as reverse annealing and it was attributed to the

formation of a new type of defects composed by carbon and nitrogen precipitates [27]. From the implantation studies of Tm and Eu implanted at RT and 500 °C, Lorenz *et al.* reported the suppression of the formation of the nanocrystalline surface layer in GaN during high-temperature implantation, a decrease of the incorporated bulk damage and an increase of the substitutional RE fraction as well as the luminescence intensity [17]. From our previous work, the damage concentration due to ion implantation in $\text{Al}_x\text{Ga}_{1-x}\text{N}$ is substantially reduced with channeled implantation up to intermediate fluences, and after thermal annealing treatment [14,28], but additional measures still need to be implemented to reduce the implantation damage.

In this work, we investigated the effect of implantation temperature on the damage accumulation and lattice deformation in $\text{Al}_x\text{Ga}_{1-x}\text{N}$. The nature of defects is investigated using transmission electron microscopy (TEM). After rapid thermal annealing, the ion channeling technique is used to unveil the lattice site location of Tb ions and photoluminescence (PL) assesses the optical activation of Tb ions within the ternary alloy.

2. Experimental details

$\text{Al}_x\text{Ga}_{1-x}\text{N}$ ($x=0.20, 0.50, 0.63$) films, grown on (0001) sapphire substrates by metal organic chemical vapor deposition (MOCVD), were purchased from NOVAGAN. The $\text{Al}_x\text{Ga}_{1-x}\text{N}$ layer thicknesses were 565 nm, 625 nm and 519 nm for samples $x=0.20, 0.50$ and 0.63, respectively. All samples were implanted with Tb ions at 150 keV and a fluence of $7 \times 10^{14} \text{ Tb.cm}^{-2}$. The implantation was carried out with the ion beam perpendicular to the sample surface normal (channeled implantation). During this process, ion channeling is guaranteed due to the high critical angle for dechanneling of 150 keV Tb ion on $\text{Al}_x\text{Ga}_{1-x}\text{N}$.

$x\text{N}$, between 6.7° and 6.1° for GaN ($x=0$) and AlN ($x=1$), respectively, according to Lindhard theory [29]. The implantation temperature was varied from RT to 550°C . Table I identifies the implantation conditions used for this study. Post-implantation rapid thermal annealing (RTA) at 1200°C in flowing N_2 during 120 s was conducted for all samples to promote the optical activation of Tb ions. The structural characterization was performed using Rutherford backscattering spectrometry/channeling (RBS/C), TEM and high-resolution X-ray diffraction (HRXRD). A 2 MeV He^+ beam delivered by a 2.5 MV Van de Graaff accelerator was used for the RBS/C measurements. The RBS/C spectra were collected with a solid state detector placed at a scattering angle of 165° with an energy resolution of 19 keV and solid angle of 11.4 msr. By rotating the sample in the azimuthal direction and tilting the sample normal by 5° away from the beam direction, random spectra were collected. A two-axes goniometer allowed crystal alignment to major crystallographic directions in order to study crystal quality and lattice site location. The determination of implantation damage profiles along the $\text{Al}_x\text{Ga}_{1-x}\text{N}$ layer depth is accomplishing using Deco code [30]. This code uses the two-beam approximation model where the incident beam is divided into dechanneled and channeled fraction that can have interaction with defects, which are considered to be randomly displaced atoms [31,32] . To account for increased dechanneling yields due to extended defects, such as stacking faults and dislocation loops, the critical angle was varied until reaching a damage level of zero in the unimplanted deeper regions of the sample [33]. Thus the derived defect profiles correspond to the density of displaced atoms leading to direct backscattering. To derive information on the density of extended defects from RBS/C spectra, detailed models of the nature of these defects need to be developed and implemented in Monte Carlo codes [34].

The Monte Carlo code FLUX was used to simulate the angular scans and extract the lattice site location of Tb ions [35]. The FLUX package is a code consisting of several programs. The most important one, called FLUX, calculates the flux density of ions inside the perfect crystal (axial channeling in the $\langle 0001 \rangle$ direction is considered in the present case). The program YIMP then uses this flux distribution to calculate the yield of impurities on certain sites inside the unit cell. By doing such simulations for different angles between the incoming ion beam and the considered crystal axis it is possible to reproduce the full channeling scan and fit it to the experimental data considering if necessary several fractions of impurities on different lattice sites.

A high-resolution D8Discover diffractometer from Bruker-AXS using Cu $K_{\alpha 1}$ radiation, a Göbel mirror, a Ge (220) monochromator, and a scintillation detector was used for the HRXRD measurements. The deformation as a function of depth was obtained by simulating and fitting the symmetric (0002) 2θ - ω scans using the dynamical theory of XRD [36] and Bartel's recursion formula [37]. The α parameter is introduced in the static structure factor to account for the decrease of diffraction intensity due to lattice defects and it is expressed by $\alpha = 1 - \exp(-\beta \cdot \varepsilon_{\perp}(z)^2)$, where β is a fitting parameter and $\varepsilon_{\perp}(z)$ is the perpendicular deformation along depth [14,28,38]. It can be interpreted as a measure of crystal quality, where it can take values between 1 (perfect crystal) and 0 (amorphous structure). The microstructure of selected samples was analyzed using TEM. Cross-section samples were prepared by mechanical polishing using a Multiprep machine to achieve a thickness lower than 10 μm . Afterwards, electron transparency was attained by 5 kV Ar ion milling using a GATAN precision ion polishing system (PIPS) at an incidence angle of 5° . During the process, the sample holder was kept at cryogenic temperature (liquid nitrogen) in order to minimize the beam damage. Observations were

carried out by conventional TEM in a JEOL 2010 (CTEM) microscope operated at 200 keV. Ion channeling is used to study the lattice site location of the implanted ions by performing angular scans across major crystallographic directions within the principal planes $\{1\bar{2}10\}$ and $\{01\bar{1}0\}$. The PL optical characterization was conducted using a 325 nm (3.8 eV) cw He-Cd laser line as the excitation source. During the measurement, the samples' temperature was varied from 14 K to RT by means of a closed-cycle helium cryostat. The luminescence was collected by a dispersive system SPEX 1704 monochromator (1 m, 1200 grooves m^{-1}) coupled to a cooled Hamamatsu R928 photomultiplier tube.

3. Results and discussion

Fig. 1 shows the $\langle 0001 \rangle$ aligned RBS/C spectra for as-grown samples and for the set of implantation temperatures studied on the three different $\text{Al}_x\text{Ga}_{1-x}\text{N}$ materials. The as-grown samples exhibit a characteristic peak at channel 600 due to the scattering of ions at the atoms in the surface plane. The surface atoms lead to a shadowing cone preventing the scattering from the underlying row of atoms. Two damage regions can be identified in all samples when analyzing the Ga-signal: surface damage within the first ~ 25 nm and the bulk damage region that can be most clearly seen for sample $x=0.20$ implanted at 100 °C and 140 °C, see Fig. 1a). It should be noted that, due to the channeled implantation geometry, the damage is already quite low at this fluence. The damage level depends on the implantation temperature and the differences are most visible for sample $x=0.20$. For this sample, both the surface and the bulk damage increase with temperature up to 140 °C and then a fast decrease is observed at 200 °C and 300 °C. At the highest temperature of

550 °C, the bulk damage increases slightly for sample $x=0.20$. For the other samples, the differences in the RBS/C spectra for varying implantation temperature are less pronounced. For all samples, the bulk damage increases for implantation at 550 °C while the surface damage is reduced.

In Fig. 2(a) the depth profile of damage accumulation extracted with the Deco code for sample $x=0.20$ is compared for three temperatures. The bulk damage has a maximum around 55 nm, close to the maximum of Tb ion distribution, as shown in the inset of Fig. 2(a). The evolution of the maximum bulk damage with implantation temperature can be followed in Fig. 2(b) for all samples. A general trend is obtained for the bulk damage in $\text{Al}_x\text{Ga}_{1-x}\text{N}$ under ion implantation at different temperatures. The damage level first increases up to temperatures of 100-200 °C and the further increase of temperature reduces it to a value close to that obtained for RT implantation. The surprising increase of damage level for implantation at 100-200°C may be related with increased interaction of defects at this temperature forming stable clusters. For 550 °C, a slight increase of damage is obtained which may be related with a less effective channeling of Tb ions due to the increase of the thermal vibrational amplitude of lattice atoms.

Fig. 3(a) shows the XRD 2θ - ω scans of the (0002) reflection and the respective simulations for samples with $x=0.20$ after implantation at different temperatures. An expansion of the c -lattice parameter in the implanted volume is evidenced by the satellite diffraction peaks appearing at lower 2θ as compared to the main Bragg peak arising from the deeper, unimplanted regions of the sample and which is similar to the peak of the as-grown sample. In accordance with RBS/C results, a higher maximum strain and lower crystal quality (α parameter) are obtained for implantation at 100 °C (and at 140 °C, not shown), while only small differences are seen for the other studied temperatures. The

perpendicular deformation and α parameter, extracted from the simulations, suggest three deformation regions along the depth; see Fig. 3(b). In the region up to 50 nm, the deformation is the highest, following the maximum of nuclear energy deposition calculated from SRIM of 20 and 30 nm for GaN and AlN, respectively [39]. In this region, no significant effect is found with temperature, except for samples implanted at 100 °C and 140 °C. For an intermediate region, between 50 nm and ~200 nm, the sample implanted at the highest temperature (550 °C) shows the lowest deformation, which could be interpreted as a low density of defects or defects of different nature. For the deepest regions, close to the deformed/non-deformed interface, the 550 °C implanted sample shows slightly higher deformation probably due to the increased defect diffusion at high temperature. Similar behavior is also observed for sample $x=0.50$. For the one with $x=0.63$, the strain at the intermediate region is reduced when the implantation is performed at temperatures above RT. In Fig. 4, the maximum perpendicular deformations, obtained from the simulation of XRD curves, are plotted to compare the effect of implantation temperature for the different AlN content samples. The same tendency is obtained for the three $\text{Al}_x\text{Ga}_{1-x}\text{N}$ layers and the evolution of $\varepsilon_{\perp}^{\text{max}}$ with temperature follows the same trend obtained for the defect concentration extracted from RBS/C; see Fig. 2(a). $\varepsilon_{\perp}^{\text{max}}$ first increases when the temperature is raised to ~100 °C, and then suffers a fast decrease between 200 °C (lowest $\varepsilon_{\perp}^{\text{max}}$ for sample $x=0.63$) and 300 °C (lowest $\varepsilon_{\perp}^{\text{max}}$ for samples $x=0.20$ and $x=0.50$). The slight increase of $\varepsilon_{\perp}^{\text{max}}$ for the highest temperature also agrees with the increase of defect concentration measured by RBS/C. Such effect may be related to the increase of thermal vibrational amplitude causing the dechanneling of implanted ions that result in more defects contributing to lattice expansion. The changes of $\varepsilon_{\perp}^{\text{max}}$, as well as the defect density obtained from RBS/C as a function of the

implantation temperature, can be explained by dynamic annealing effects. Point defects created in GaN by ion implantation were shown to be mobile at temperatures below RT [8]. Increasing the temperature is expected to increase their mobility, which can enhance defect recombination as well as the interaction of point defects among each other. RBS/C and XRD results thus suggest that raising the implantation temperature to ~ 100 - 200°C enhances the interaction between defects and promotes the formation of stable complex defects. Further increase in the implantation temperature either leads to a reduction of the complex defects concentration or to a transformation of defects morphology (i.e. the formation of defects for which RBS/C and XRD are less sensitive).

In order to shed more light on these issues, two samples $x=0.20$ implanted at 100 and 550°C were further investigated by TEM. In Fig. 5(a) the $g=0002$ weak beam image for the sample implanted at 100°C shows contrast related to interstitial or vacancy clusters down to ~ 150 nm. From $g=10\bar{1}0$ weak beam image, a buried layer of 60 nm width shows non-continuous bright lines parallel to the sample surface related to stacking faults, while the surface layer (18 nm) exhibits no stacking faults, see Fig 5(b). These results are very similar to those reported on implanted III-nitrides at RT [13,15,40,41]. In particular, GaN, AlN and $\text{Al}_x\text{Ga}_{1-x}\text{N}$ implanted with RE at RT showed the coexistence of defect clusters and basal stacking faults [14,19,42]. Therefore, we conclude that raising the implantation temperature to 100°C increases the concentration of these defects but does not change their nature when compared to samples implanted at RT. When the implantation is performed at 550°C , the profile of defect clusters with displacements along the c -axis extends to deeper regions (200 nm) due to the increase of defect diffusion at high temperature, see Figure 6(a). Interestingly, the formation of stacking faults is suppressed at this implantation temperature, indicating the beneficial contribution of defect diffusion,

as shown in Fig. 6(b). This is clearly an effect of altered dynamic annealing processes since much higher temperatures are required to remove stacking faults once they are formed (well above 1000°C in GaN) [43].

Additional characterization should be performed in order to understand the processes leading to increased damage formation at 100-200 °C. Previous studies performed for GaN also showed the increase of damage concentration but in a different temperature range, between 500 °C and 700 °C. This behavior was attributed to the formation of a new type of defects composed by carbon and nitrogen precipitates [27]. In fact, carbon contamination is possible due to the decomposition of organic radicals during the crystal growth by MOCVD. The growth of AlGaIn by MOCVD involves a chemical reaction of vapor-phase metal-organic precursors such as trimethyl or triethyl gallium/aluminum as Ga and Al sources while ammonia (N source) is used as a reactant gas [44,45]. Carbon contamination is possible when residual compounds originated in the partial dissociation of trimethyl or triethyl gallium/aluminum precursors to dimethyl group, which can end being absorbed on the growing surface [46,47]. An increase of damage accumulation around 100 °C was also reported for GaN by Pipeleers [41], although it was more pronounced for random implantation geometry. In the same work, the strain profile was consistent with the defect concentration up to 500 °C, and after that, an increase of strain attributed to the formation of nitrogen bubbles or precipitates was found.

The samples were annealed at 1200 °C during 120 s to promote the recovery of implantation damage and to optically activate the implanted ions. Fig. 7 shows the remaining damage concentration measured by RBS/C after the thermal treatment. Although not completely removed, the damage is reduced in all the samples with the exception of the ones with $x=0.63$ and implanted at RT and 100 °C, which showed lower

defect accumulation before the annealing treatment (see Fig. 2(b)). This is similar to results reported for Eu implanted AlN where in samples with very low defect concentrations (low fluences comparable to those used here) the damage was seen to increase slightly after annealing, possibly due to the formation of defect complexes [19]. Independently of AlN molar fraction, the final lattice disorder remains higher for samples implanted at 100 °C, as it was already the case for as-implanted samples.

Fig. 8(a) shows the HRXRD measurements of 2θ - ω scans of (0002) reflection for selected $x=0.20$ samples. The lattice deformation is reduced after thermal annealing (compare with Fig. 3(a)) but the highest deformation is still observed for the sample implanted at 100 °C, in agreement with RBS/C results. The lattice perpendicular deformation for the same samples is shown in Fig. 8(b). The inset shows the α parameter depth profiles. The lattice deformation profile is similar for the implantation temperatures studied with the exception of the sample implanted at 100 °C, which shows higher deformation but a lower volume of deformed material. All samples showed a recovery of the deepest implanted region, evident by the reduced thickness of the deformed layer. For the remaining temperatures, the maximum of deformation is similar and the extension reaches up to 300 nm of depth. The comparison of $\varepsilon_{\perp}^{\max}$ for all the samples after thermal annealing is depicted in Fig. 9. The $\varepsilon_{\perp}^{\max}$ decreases for all the samples in comparison with the as-implanted state and the trend is similar for the different AlN content samples. However, for sample $x=0.50$ a decrease of $\varepsilon_{\perp}^{\max}$ is seen with the increase of implantation temperature starting from 100 °C, while the behavior of as-implanted samples is kept for the other samples with different AlN content. It can be seen that lower deformation is obtained when implantation temperature is increased, and the lowest values are obtained for 300 °C ($x=0.20$), 550 °C ($x=0.50$) and 200 °C ($x=0.63$). Interestingly, the same tendency as obtained for the defect

concentration extracted from RBS/C (Fig. 7) is observed for lattice deformation. However, the agreement is not perfect. For example, for 100°C implantation the sample $x=0.2$ shows the lowest density of displaced atoms measured by RBS/C while the strain is still higher than for sample $x=0.63$. This should be due to different sensitivities of the two techniques for certain defect types. Sample $x=0.20$ implanted at 100 °C and annealed at 1200 °C was also investigated from the microstructural point of view with TEM. The $g=10\bar{1}0$ image is shown in Fig. 10, revealing the contrast related to basal stacking faults (some are marked with white arrows) but showing lower density of such basal defects as compared to the as-implanted sample (Fig. 5(b)). This is in agreement with the reduction of stacking fault density in ion-implanted GaN annealed at the same temperature [43]. For the TEM images along $g=0002$ (not shown), no noticeable difference was obtained but quantification of defect complex concentration by TEM is difficult.

Tb lattice site location was investigated for selected samples after thermal annealing treatment. Fig. 11 shows the full angular scans for the $x=0.20$ sample implanted at the highest temperature (550 °C) for the $\langle 0001 \rangle$ axis as well as two tilted axes, within different families of planes, $\langle \bar{2}113 \rangle$ in $\{01\bar{1}0\}$ and $\langle 01\bar{1}0 \rangle$ in $\{12\bar{1}0\}$. Flux simulations were performed to extract the position of Tb ions within the $\text{Al}_x\text{Ga}_{1-x}\text{N}$ lattice. A good agreement of the simulation with the experimental results for the Ga sublattice was found, assuming a lattice vibration amplitude u_2 of 0.09 Å. The best fit for the Tb scan was achieved considering two different lattice sites (a substitutional cation site, F_s , and a site displaced by 0.2 Å along c -axis from the substitutional site, F_d) plus a fraction of randomly distributed atoms, F_{ran} . The best fit obtained for this sample was achieved considering F_s of 70(4) %, F_d of 17(3) % and F_{ran} of 13(1) %. For the $x=0.20$ sample implanted at RT, the results obtained do not differ much from the high implantation

temperature sample, with the best fit achieved with F_s of 63(5) %, F_{ran} of 10(1) % and a higher fraction of Tb ions displaced along the c -axis (27(4) %). The displacement of 0.2 Å is consistent with the displacements found in a previous work where the Tb ion implantation in $Al_xGa_{1-x}N$ was performed at RT [42]. Sample $x=0.50$ implanted at 550 °C was also studied after annealing. The FLUX simulation revealed a similar site location and fractions, as obtained for sample $x=0.20$ implanted at the same temperature ($F_s = 74$ %, $F_d = 13$ %, $F_{ran} = 13$ %). It should be noted that the defect concentration (Fig. 7) and the maximum perpendicular deformation (Fig. 9) are similar for both samples. The Tb fraction found on the displaced site may be related to the formation of defect complexes such as Tb substituting a cation plus a next neighbor nitrogen vacancy ($RE_{Al/Ga} + V_N$). Theoretical calculation considering Er, Eu and Tm ions in GaN and using Density Functional Theory showed that these defect complexes have high binding energy and that the two possible defect configurations, axial and basal depending on V_N position, lead to the relaxation of RE (by 0.1 to 0.2 Å) towards the vacancy [37–39]. Axial configuration agrees with the displacement along the c -direction obtained in this work and the high binding energy (1.1 eV to 1.6 eV) may explain its stability even after thermal annealing [50].

The samples implanted at different temperatures were optically studied using PL (Fig. 12), under excitation of 325 nm (above bandgap for $x=0.20$ and below for the remaining AlN molar fractions). Fig. 12 (a) shows the low temperature PL spectra for the $Al_xGa_{1-x}N$ sample with $x=0.20$ before and after implantation at 300 °C (with 7×10^{14} Tb.cm⁻²) and annealing at 1200 °C. For the as-grown samples, sharp lines of unknown origin are observed in the ultraviolet region, as well as, a broad yellow luminescence band (YB) in the visible region. After implantation, a broad UV band is detected, likely due to the

defects generated during the implantation process. The optical activation of Tb^{3+} was only achieved after the thermal treatment, revealing the intraionic transitions of Tb^{3+} assigned to $^5\text{D}_4 \rightarrow ^7\text{F}_J$ with $J=6, 5, 4$ and 3 (shown in Fig. 12 (b)). The highest peak intensity was observed for the $^5\text{D}_4 \rightarrow ^7\text{F}_6$ transition, at ~ 491 nm. These transitions appear overlapped with the YB. A slight shift of this band from ~ 525 nm (as-grown sample) to ~ 541 nm was observed, which may be attributed to different relative intensities of the optically active centers that contribute to this emission. Furthermore, previous works revealed that thermal annealing may induce/promote the defects responsible for the YB [53], which seems to be also the case in the present samples.

As previously mentioned, the samples were implanted at different temperatures and a comparison of the PL spectra for sample $x=0.20$ is depicted in Fig. 12 (b). This sample was chosen for this comparison since it is the one that showed the best lattice recovery after thermal annealing. Additionally, only for this composition does the used laser allow the excitation above the bandgap. An increase in the relative intensity of the intraionic emission is clearly observed with increasing implantation temperature. Since the relative damage concentration was found to be slightly higher for the sample implanted at 550°C , this increase is likely due to the presence of a higher concentration of Tb^{3+} ions on substitutional cation sites for this implantation temperature.

Fig. 12 (c) shows the RT PL spectra for the three AlN compositions and implanted at 550°C . In the case of the samples with higher AlN molar fraction ($x=0.50$ and 0.63) a broad band centered around 500 nm is also visible. For those samples, the intraionic Tb emission is mostly obscured by this band since its relative intensity is very weak. As this band was not present in the as-grown samples (not shown), its origin should be related

with the defects created during implantation and/or annealing processes. In fact, these samples exhibit a higher relative damage concentration when compared to the $x=0.20$ sample (see Fig. 7). Thus, the ion may be surrounded by a higher concentration of damage sites that contribute for the quenching of the intraionic emission. However, different excitation pathways for excitation below the bandgap may also play a role in the exhibited spectral shape.

Conclusions

$\text{Al}_x\text{Ga}_{1-x}\text{N}$ films grown by MOCVD were implanted with Tb ions at a fluence of 7×10^{14} Tb.cm^{-2} under channeled geometry. In pursuance of further implantation damage reduction, the substrate temperature was raised during ion implantation as a way to increase defect mobility that results in the recombination of vacancies and interstitials; the implantation temperature was varied from RT to 550 °C. The bimodal damage distribution has a different behavior with increasing temperature for the two damage regions: at the near-surface and at the bulk. The near-surface damage decreases with increasing temperature for high AlN content samples, while for the lower AlN content it first increases up to 140 °C and then decreases with temperature. The bulk damage follows the same trend for different $\text{Al}_x\text{Ga}_{1-x}\text{N}$ under ion implantation with increasing implantation temperature. The increase of temperature to ~100-200 °C increases the damage accumulation and the further increase of temperature reduces it down to a value close to the damage obtained at RT. A twofold effect at high temperature should be considered: the increase of the thermal vibrational amplitude of lattice atoms which decreases the channeling of implanted ions and the increase of defect diffusion. The former hampers the

further damage reduction, as observed from RBS/C and XRD for implantation at 550°C, while the latter may be related with the suppression of basal stacking faults at this implantation temperature. In contrast, implantation at 100 °C, results in an increase of defect concentration and strain as measured by RBS/C and XRD while the dominant defects visible in TEM images are the same as in RT-implanted samples, namely, point defect clusters and basal stacking faults. The evolution of the maximum of perpendicular deformation with temperature follows the trend observed for the defect concentration extracted from RBS/C in all samples before and after annealing. Thermal annealing partially reduces the implantation damage and the microstructural changes result in the decrease of basal stacking fault density without much change for the atomic displacements along *c*-axis. The *c*-lattice expansion is also reduced and the same tendency as obtained for the defect concentration extracted from RBS/C is observed for the lattice deformation. Tb lattice site location for samples implanted at different temperature and after thermal annealing revealed a similar signature in all the investigated samples, with a slightly higher Tb fraction on substitutional cation sites found for the implantation performed at 550 °C. The characteristic green light emission from Tb³⁺ ⁵D₄ → ⁷F₆ emitting level is achieved for all the Al_xGa_{1-x}N samples.

Acknowledgements

We acknowledge financial support from PEST-OE/CTM-UI0084/2011 contract and Fundação para a Ciência e Tecnologia of individual grants of M Fialho (SFRH/BD/78740/2011) and S Magalhães (SRFH/BPD/98738/2013).

References

- [1] T.J. Flack, B.N. Pushpakaran, S.B. Bayne, GaN Technology for Power Electronic Applications: A Review, *J. Electron. Mater.* 45 (2016) 2673–2682. doi:10.1007/s11664-016-4435-3.
- [2] M.T. Hardy, D.F. Feezell, S.P. DenBaars, S. Nakamura, Group III-nitride lasers: a materials perspective, *Mater. Today*. 14 (2011) 408–415. doi:10.1016/S1369-7021(11)70185-7.
- [3] A. Khan, K. Balakrishnan, T. Katona, Ultraviolet light-emitting diodes based on group three nitrides, *Nat. Photonics*. 2 (2008) 77–84. doi:10.1038/nphoton.2007.293.
- [4] K.P. O'Donnell, M. Auf der Maur, A. Di Carlo, K. Lorenz, the SORBET consortium, It's not easy being green: Strategies for all-nitrides, all-colour solid state lighting, *Phys. Status Solidi RRL – Rapid Res. Lett.* 6 (2012) 49–52. doi:10.1002/pssr.201100206.
- [5] L. Zhang, C. Liu, White light emission from GaN stack layers doped by different rare-earth metals, *Jpn. J. Appl. Phys.* 54 (2015) 02BA03. doi:10.7567/JJAP.54.02BA03.
- [6] R. Dahal, C. Ugolini, J.Y. Lin, H.X. Jiang, J.M. Zavada, Erbium-doped GaN optical amplifiers operating at 1.54 μm , *Appl. Phys. Lett.* 95 (2009) 111109. doi:10.1063/1.3224203.
- [7] L.A. Larson, J.M. Williams, M.I. Current, Ion Implantation for Semiconductor Doping and Materials Modification, *Rev. Accel. Sci. Technol.* 04 (2011) 11–40. doi:10.1142/S1793626811000616.
- [8] K. Lorenz, M. Peres, N. Franco, J.G. Marques, S.M.C. Miranda, S. Magalhães, T. Monteiro, W. Wesch, E. Alves, E. Wendler, Radiation damage formation and annealing in GaN and ZnO, *Proc. of SPIE Vol. 7940* (2011) 79400O. doi:10.1117/12.879402.

- [9] S.O. Kucheyev, J.S. Williams, J. Zou, G. Li, C. Jagadish, M.O. Manasreh, M. Pophristic, S. Guo, I.T. Ferguson, Structural disorder in ion-implanted $\text{Al}_x\text{Ga}_{1-x}\text{N}$, *Appl. Phys. Lett.* 80 (2002) 787–789. doi:10.1063/1.1445478.
- [10] A. Turos, On the mechanism of damage buildup in gallium nitride, *Radiat. Eff. Defects Solids*. 168 (2013) 431–441. doi:10.1080/10420150.2013.777445.
- [11] K. Pałowska, R. Ratajczak, A. Stonert, L. Nowicki, A. Turos, Compositional dependence of damage buildup in Ar-ion bombarded AlGaIn , *Vacuum*. 83, Supplement 1 (2009) S145–S147. doi:10.1016/j.vacuum.2009.01.048.
- [12] D.N. Faye, E. Wendler, M. Felizardo, S. Magalhães, E. Alves, F. Brunner, M. Weyers, K. Lorenz, Mechanisms of Implantation Damage Formation in $\text{Al}_x\text{Ga}_{1-x}\text{N}$ Compounds, *J. Phys. Chem. C*. 120 (2016) 7277–7283. doi:10.1021/acs.jpcc.6b00133.
- [13] P. Ruterana, M.-P. Chauvat, K. Lorenz, Mechanisms of Damage Formation during Rare Earth Ion Implantation in Nitride Semiconductors, *Jpn. J. Appl. Phys.* 52 (2013) 11NH02. doi:10.7567/JJAP.52.11NH02.
- [14] M. Fialho, S. Magalhães, M.P. Chauvat, P. Ruterana, K. Lorenz, E. Alves, Impact of implantation geometry and fluence on structural properties of $\text{Al}_x\text{Ga}_{1-x}\text{N}$ implanted with thulium, *J. Appl. Phys.* 120 (2016) 165703. doi:10.1063/1.4966120.
- [15] S.O. Kucheyev, J.S. Williams, J. Zou, C. Jagadish, Dynamic annealing in III-nitrides under ion bombardment, *J. Appl. Phys.* 95 (2004) 3048–3054. doi:10.1063/1.1649459.
- [16] K. Lorenz, S.M.C. Miranda, E. Alves, I.S. Roqan, K.P. O'Donnell, M. Boćkowski, High pressure annealing of Europium implanted GaIn , *Proc. of SPIE* 8262, (2012) 82620C. doi:10.1117/12.906810.
- [17] K. Lorenz, U. Wahl, E. Alves, E. Nogales, S. Dalmaso, R.W. Martin, K.P. O'Donnell, M. Wojdak, A. Braud, T. Monteiro, T. Wojtowicz, P. Ruterana, S. Ruffenach,

- O. Briot, High temperature annealing of rare earth implanted GaN films: Structural and optical properties, *Opt. Mater.* 28 (2006) 750–758. doi:10.1016/j.optmat.2005.09.015.
- [18] A. Vantomme, S.M. Hogg, M.F. Wu, B. Pipeleers, M. Swart, S. Goodman, D. Aurret, K. Iakoubovskii, G.J. Adriaenssens, K. Jacobs, I. Moerman, Suppression of rare-earth implantation-induced damage in GaN, *Nucl. Instrum. Methods Phys. Res. Sect. B Beam Interact. Mater. At.* 175–177 (2001) 148–153. doi:10.1016/S0168-583X(00)00550-4.
- [19] K. Lorenz, E. Alves, F. Gloux, P. Ruterana, M. Peres, A.J. Neves, T. Monteiro, Optical doping and damage formation in AlN by Eu implantation, *J. Appl. Phys.* 107 (2010) 023525. doi:10.1063/1.3291100.
- [20] J. Nord, K. Nordlund, B. Pipeleers, A. Vantomme, Implantation angle dependence of ion irradiation damage in GaN, *Mater. Sci. Eng. B.* 105 (2003) 111–113. doi:10.1016/j.mseb.2003.08.026.
- [21] S.F. Song, W.D. Chen, J. Zhu, C.C. Hsu, Dependence of implantation-induced damage with photoluminescence intensity in GaN:Er, *J. Cryst. Growth.* 265 (2004) 78–82. doi:10.1016/j.jcrysgro.2004.01.056.
- [22] B. Pipeleers, S.M. Hogg, A. Vantomme, Defect accumulation during channeled erbium implantation into GaN, *J. Appl. Phys.* 98 (2005) 123504. doi:10.1063/1.2143120.
- [23] B. Pipeleers, S.M. Hogg, A. Vantomme, Influence of the implantation angle on the generation of defects for Er implanted GaN, *Nucl. Instrum. Methods Phys. Res. Sect. B Beam Interact. Mater. At.* 206 (2003) 95–98. doi:10.1016/S0168-583X(03)00689-X.
- [24] N. Parikh, A. Suvkhanov, M. Lioubtchenko, E. Carlson, M. Bremser, D. Bray, R. Davis, J. Hunn, Ion implantation of epitaxial GaN films: damage, doping and activation, *Nucl. Instrum. Methods Phys. Res. Sect. B Beam Interact. Mater. At.* 127 (1997) 463–466. doi:10.1016/S0168-583X(97)00076-1.

- [25] W. Jiang, W.J. Weber, Effect of irradiation temperature on dynamic recovery in gallium nitride, *Nucl. Instrum. Methods Phys. Res. B.* 242 (2006) 431–433. doi:10.1016/j.nimb.2005.08.163.
- [26] I. Usov, N. Parikh, D.B. Thomson, R.F. Davis, Effect Of Implantation Temperature On Damage Accumulation In Ar - Implanted GaN, *Mater. Res. Soc. Internet J. Nitride Semicond. Res.* 7 (2002). doi:10.1557/S1092578300000351.
- [27] I. Usov, A. Kvit, Z. Reitmeier, R. Davis, Radiation Damage Characterization in Ar Implanted GaN, *MRS Online Proc. Libr. Arch.* 792 (2003). doi:10.1557/PROC-792-R9.4.
- [28] S. Magalhães, M. Fialho, M. Peres, K. Lorenz, E. Alves, Quantitative x-ray diffraction analysis of bimodal damage distributions in Tm implanted Al 0.15 Ga 0.85 N, *J. Phys. Appl. Phys.* 49 (2016) 135308. doi:10.1088/0022-3727/49/13/135308.
- [29] R.C. Bird, J.S. Williams, eds., *Ion Beams for Materials Analysis*, 1 edition, Academic Press, Sydney; San Diego, 1989.
- [30] E. Wendler, W. Wesch, G. Götz, Radiation damage and optical properties of Ar+-implanted GaP, *J. Appl. Phys.* 70 (1991) 144–149. doi:10.1063/1.350302.
- [31] G. Goetz, *High Energy Ion Beam Analysis of Solids*, Vch Pub, Berlin, 1988.
- [32] E. Albertazzi, M. Bianconi, G. Lulli, R. Nipoti, M. Cantiano, Different methods for the determination of damage profiles in Si from RBS-channeling spectra: a comparison, *Nucl. Instrum. Methods Phys. Res. Sect. B Beam Interact. Mater. At.* 118 (1996) 128–132. doi:10.1016/0168-583X(95)01489-6.
- [33] K. Lorenz, E. Wendler, A. Redondo-Cubero, N. Catarino, M.-P. Chauvat, S. Schwaiger, F. Scholz, E. Alves, P. Ruterana, Implantation damage formation in a-, c- and m-plane GaN, *Acta Mater.* 123 (2017) 177–187. doi:10.1016/j.actamat.2016.10.020.

- [34] A. Turos, P. Jóźwik, M. Wójcik, J. Gaca, R. Ratajczak, A. Stonert, Mechanism of damage buildup in ion bombarded ZnO, *Acta Mater.* 134 (2017) 249–256.
doi:10.1016/j.actamat.2017.06.005.
- [35] P.J.M. Smulders, D.O. Boerma, Computer simulation of channeling in single crystals, *Nucl. Instrum. Methods Phys. Res. Sect. B Beam Interact. Mater. At.* 29 (1987) 471–489.
doi:10.1016/0168-583X(87)90058-9.
- [36] A. Authier, *Dynamical Theory of X-Ray Diffraction*, Revised edition, Oxford University Press, 2004.
- [37] W.J. Bartels, J. Hornstra, D.J.W. Lobeek, X-ray diffraction of multilayers and superlattices, *Acta Crystallogr. A.* 42 (1986) 539–545. doi:10.1107/S0108767386098768.
- [38] N. Sousbie, L. Capello, J. Eymery, F. Rieutord, C. Lagahe, X-ray scattering study of hydrogen implantation in silicon, *J. Appl. Phys.* 99 (2006) 103509.
doi:10.1063/1.2198928.
- [39] J.P. Biersack, J.F. Ziegler, The Stopping and Range of Ions in Solids, in: D.H. Ryssel, D.H. Glawischnig (Eds.), *Ion Implant. Tech.*, Springer Berlin Heidelberg, 1982: pp. 122–156. doi:10.1007/978-3-642-68779-2_5.
- [40] F. Gloux, T. Wojtowicz, P. Ruterana, K. Lorenz, E. Alves, Transmission electron microscopy investigation of the structural damage formed in GaN by medium range energy rare earth ion implantation, *J. Appl. Phys.* 100 (2006) 073520.
doi:10.1063/1.2357845.
- [41] S.O. Kucheyev, J.S. Williams, J. Zou, C. Jagadish, M. Pophristic, S. Guo, I.T. Ferguson, M.O. Manasreh, Ion-beam-produced damage and its stability in AlN films, *J. Appl. Phys.* 92 (2002) 3554–3558. doi:10.1063/1.1501746.

- [42] P. Ruterana, B. Lacroix, K. Lorenz, A mechanism for damage formation in GaN during rare earth ion implantation at medium range energy and room temperature, *J. Appl. Phys.* 109 (2011) 013506. doi:10.1063/1.3527944.
- [43] T. Wójtowicz, F. Gloux, P. Ruterana, K. Lorenz, E. Alves, TEM investigation of Tm implanted GaN, the influence of high temperature annealing, *Opt. Mater.* 28 (2006) 738–741. doi:10.1016/j.optmat.2005.09.012.
- [44] Y. Ohba, H. Yoshida, R. Sato, Growth of High-Quality AlN, GaN and AlGaIn with Atomically Smooth Surfaces on Sapphire Substrates, *Jpn. J. Appl. Phys.* 36 (1997) L1565. doi:10.1143/JJAP.36.L1565.
- [45] B. Liu, R. Zhang, Z.L. Xie, Q.J. Liu, Z. Zhang, Y. Li, X.Q. Xiu, J. Yao, Q. Mei, H. Zhao, P. Han, H. Lu, P. Chen, S.L. Gu, Y. Shi, Y.D. Zheng, W.Y. Cheung, N. Ke, J.B. Xu, Al incorporation, structural and optical properties of $\text{Al}_x\text{Ga}_{1-x}\text{N}$ ($0.13 \leq x \leq 0.8$) alloys grown by MOCVD, *J. Cryst. Growth.* 310 (2008) 4499–4502. doi:10.1016/j.jcrysgro.2008.07.076.
- [46] F.J. Lumbantoruan, Y.-Y. Wong, W.-C. Huang, H.-W. Yu, E.-Y. Chang, Effects of NH_3 Flow Rate During AlGaIn Barrier Layer Growth on the Material Properties of AlGaIn/GaN HEMT Heterostructure, *J. Electron. Mater.* 46 (2017) 6104–6110. doi:10.1007/s11664-017-5550-5.
- [47] G. Parish, S. Keller, S.P. Denbaars, U.K. Mishra, SIMS investigations into the effect of growth conditions on residual impurity and silicon incorporation in GaN and $\text{Al}_x\text{Ga}_{1-x}\text{N}$, *J. Electron. Mater.* 29 (2000) 15–20. doi:10.1007/s11664-000-0087-3.
- [48] B. Pipeleers, Defect Accumulation in Erbium Implanted Gallium Nitride, Ph.D., KU Leuven, 2005.

- [49] M. Fialho, J. Rodrigues, S. Magalhães, M.R. Correia, T. Monteiro, K. Lorenz, E. Alves, Effect of AlN content on the lattice site location of terbium ions in $\text{Al}_x\text{Ga}_{1-x}\text{N}$ compounds, *Semicond. Sci. Technol.* 31 (2016) 035026. doi:10.1088/0268-1242/31/3/035026.
- [50] S. Sanna, B. Hourahine, T. Frauenheim, U. Gerstmann, Theoretical study of rare earth point defects in GaN, *Phys. Status Solidi C*. 5 (2008) 2358–2360. doi:10.1002/pssc.200778667.
- [51] S. Sanna, W.G. Schmidt, T. Frauenheim, U. Gerstmann, Rare-earth defect pairs in GaN: LDA+U calculations, *Phys. Rev. B*. 80 (2009) 104120. doi:10.1103/PhysRevB.80.104120.
- [52] J.-S. Filhol, R. Jones, M.J. Shaw, P.R. Briddon, Structure and electrical activity of rare-earth dopants in GaN, *Appl. Phys. Lett.* 84 (2004) 2841–2843. doi:10.1063/1.1710710.
- [53] J. Rodrigues, S.M.C. Miranda, A.J.S. Fernandes, E. Nogales, L.C. Alves, E. Alves, G. Tourbot, T. Auzelle, B. Daudin, B. Méndez, T. Trindade, K. Lorenz, F.M. Costa, T. Monteiro, Towards the understanding of the intentionally induced yellow luminescence in GaN nanowires, *Phys. Status Solidi C*. 10 (2013) 667–672. doi:10.1002/pssc.201200714.

Tables

Table I: Experimental conditions used for the implantation of Tb ions in $\text{Al}_x\text{Ga}_{1-x}\text{N}$ layers.

$\text{Al}_x\text{Ga}_{1-x}\text{N}$	Temperature (°C)	Fluence ($\text{Tb}\cdot\text{cm}^{-2}$)	Angle (deg.)	Energy (keV)
x=0.20, 0.5, 0.63	RT	7×10^{14}	0	150
x=0.20	70			
x=0.20, 0.5, 0.63	100			
x=0.20	140			
x=0.20, 0.5, 0.63	200			
x=0.20, 0.5, 0.63	300			
x=0.20, 0.5, 0.63	550			

List of figure captions:

Fig. 1: $\langle 0001 \rangle$ RBS/C spectra for samples (a) $x=0.20$, (b) $x=0.50$ and (c) $x=0.63$ implanted to a fluence of 7×10^{14} Tb.cm $^{-2}$ at temperatures ranging from RT to 550 °C and under channelled geometry. The regions of bulk damage and surface damage are indicated on the depth scale.

Fig. 2: (a) Relative damage concentration as a function of depth for sample $x=0.20$ implanted with 7×10^{14} Tb.cm $^{-2}$ at different temperatures. The inset shows the Tb depth profile. (b) Relative damage concentration as a function of implantation temperature taken at the maximum of the bulk damage region at about 55 nm depth as indicated in a).

Fig. 3: (a) HRXRD 2θ - ω scans of (0002) reflection for samples with $x=0.20$ implanted with Tb ions at different temperatures and (b) the perpendicular deformation profile extracted from the simulation of XRD curves. The inset shows the α parameter depth profile.

Fig. 4: Maximum perpendicular deformation as a function of implantation temperature for Al $_x$ Ga $_{1-x}$ N samples with $x=0.20$, 0.50 and 0.63 implanted with a terbium fluence of 7×10^{14} Tb.cm $^{-2}$.

Fig. 5: Cross-sectional TEM dark field observations using (a) $g=0002$ and (b) $g=10\bar{1}0$ reflections in weak beam condition for sample $x=0.20$ after Tb implantation at 100 °C.

Fig. 6: Cross-sectional TEM dark field observations using (a) $g=0002$ and (b) $g=10\bar{1}0$ reflections in weak beam condition for sample $x=0.20$ after Tb implantation at 550 °C.

Fig. 7: Relative damage concentration as a function of implantation temperature taken at the maximum of the bulk damage region.

Fig. 8: (a) HRXRD 2θ - ω scans of (0002) reflection for samples with $x=0.20$ implanted with Tb ions at implantation at different temperatures and after rapid thermal annealing at 1200 °C and (b) the perpendicular deformation profile extracted from the simulation of XRD curves. The inset shows the α parameter depth profile.

Fig. 9: Maximum perpendicular deformation as a function of implantation temperature for $\text{Al}_x\text{Ga}_{1-x}\text{N}$ samples with $x=0.20$, 0.50 and 0.63 implanted with a terbium fluence of 7×10^{14} Tb.cm^{-2} and annealed at 1200 °C.

Fig. 10: Cross-sectional TEM dark field images using $g=10\bar{1}0$ reflections in weak beam condition for sample $x=0.20$ after Tb implantation at 100 °C and subsequent thermal annealing treatment. The arrows indicate some of the basal stacking faults.

Fig. 11: Full angular scans across $\langle 0001 \rangle$, $\langle \bar{2}113 \rangle$ and $\langle 10\bar{1}1 \rangle$ crystallographic directions sample $x=0.20$ implanted at 550 °C and annealed at 1200 °C.

Fig. 12: (a) Comparison of the 14 K PL spectra for the $\text{Al}_{0.2}\text{Ga}_{0.8}\text{N: Tb}^{3+}$ sample before and after implantation at 300 °C and annealing at 1200 °C. (b) 14 K PL spectra for sample $x=0.20$ implanted at different temperatures and annealed at 1200 °C. (c) RT PL spectra for $\text{Al}_x\text{Ga}_{1-x}\text{N: Tb}^{3+}$ ($0.20 \leq x \leq 0.63$) samples, implanted at 550 °C and annealed at 1200 °C. The emission lines of Tb^{3+} are indicated by arrows.

Figures

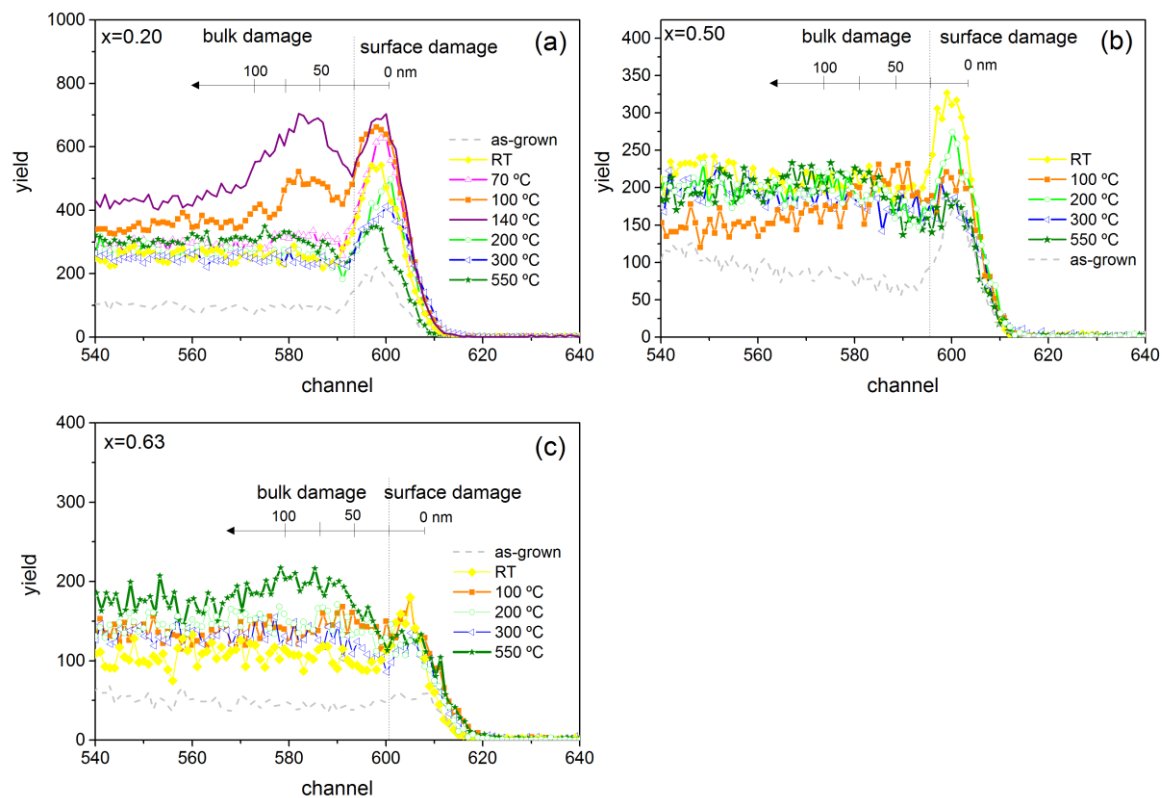


Fig. 1

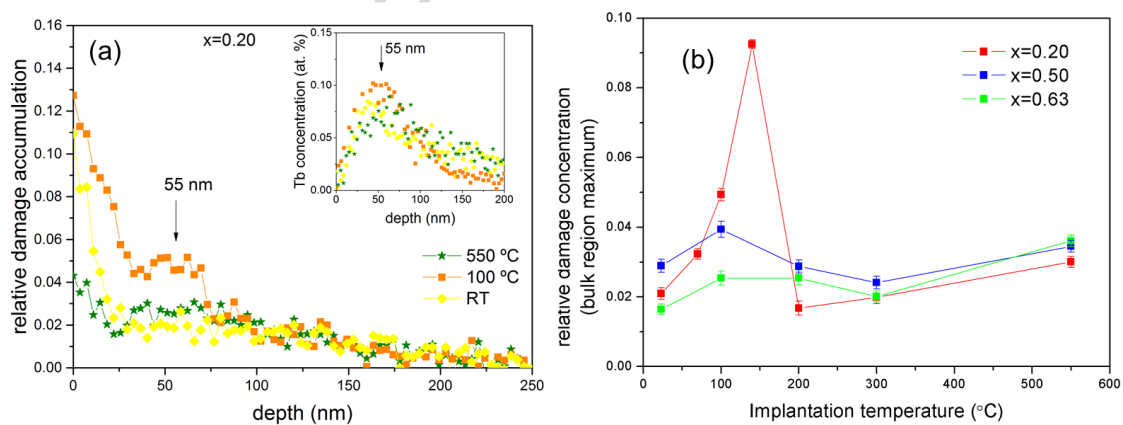


Fig. 2

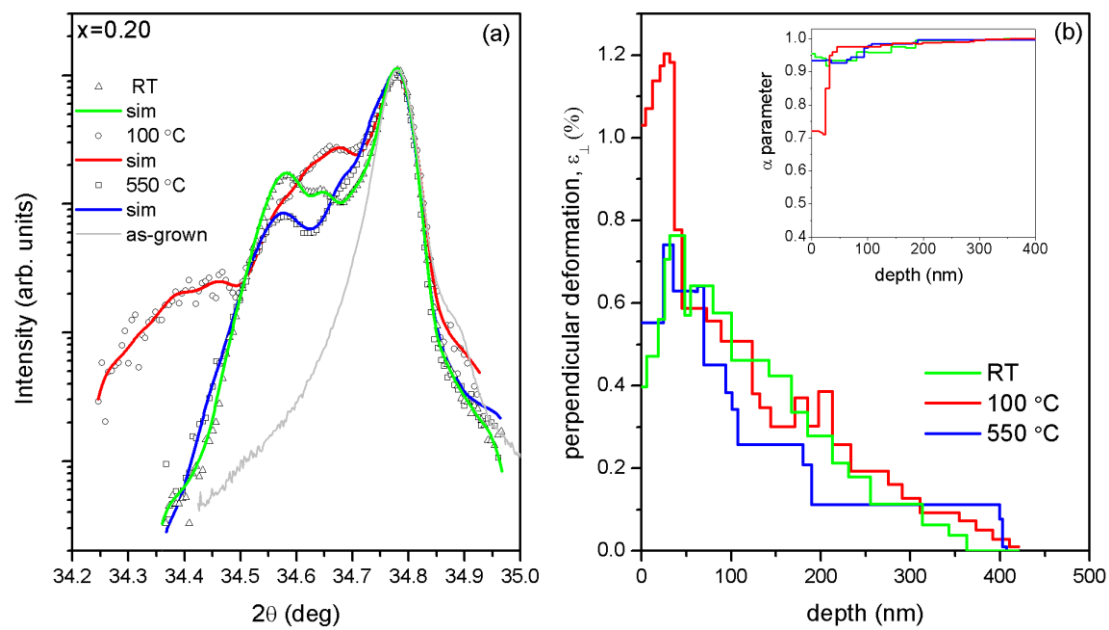


Fig. 3

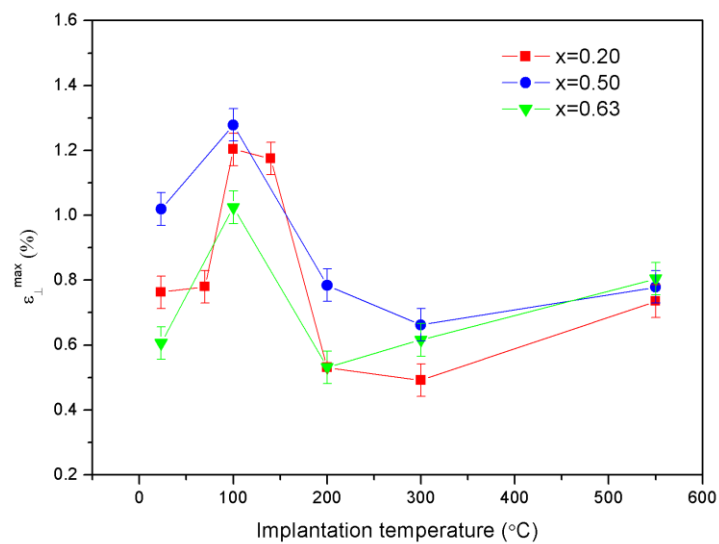


Fig. 4

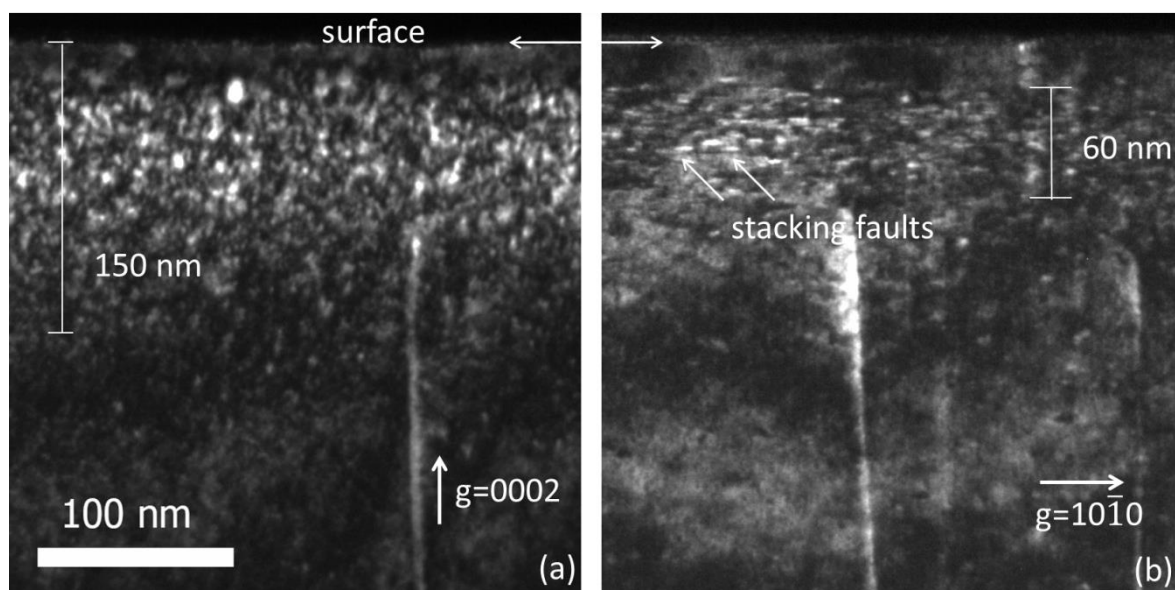


Fig. 5

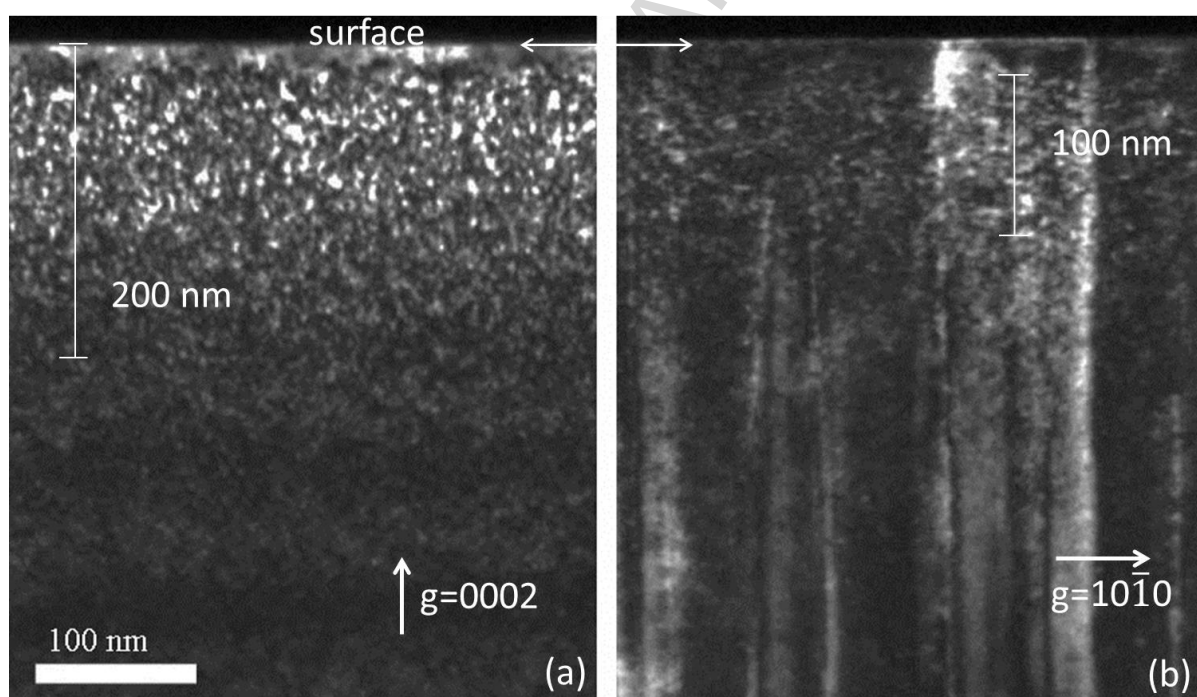


Fig. 6

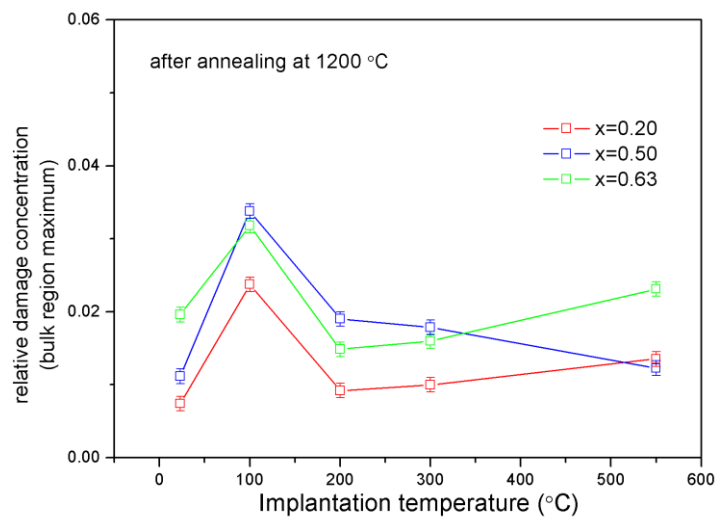


Fig. 7

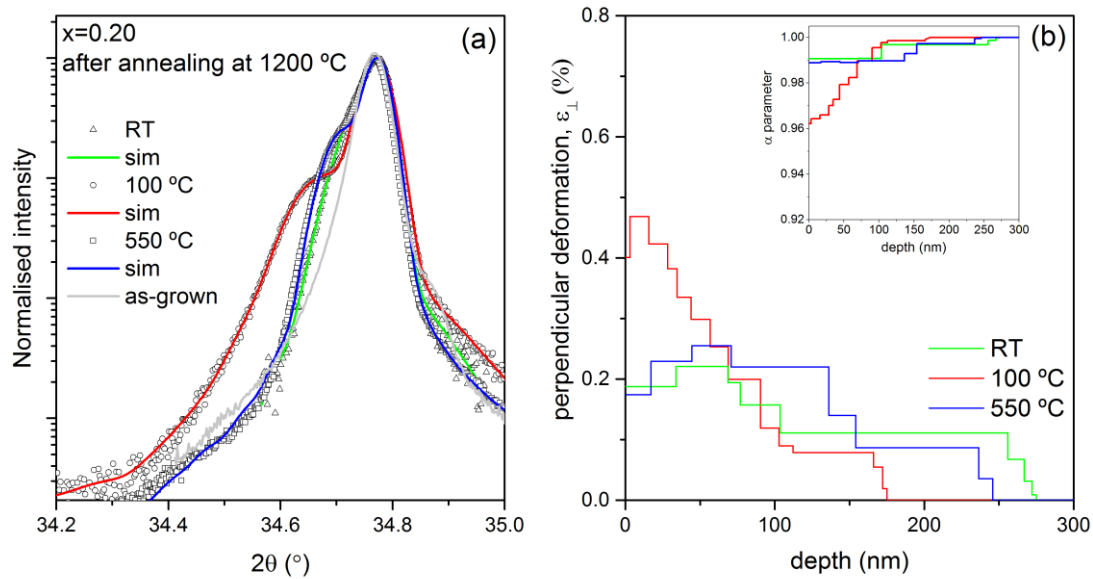


Fig. 8

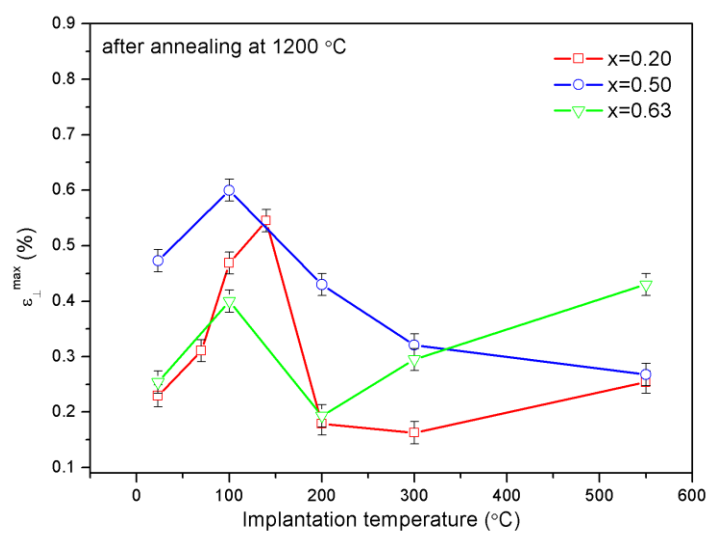


Fig. 9

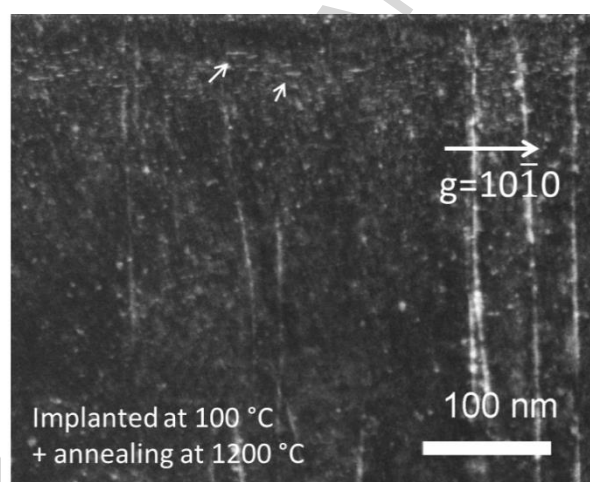


Fig. 10

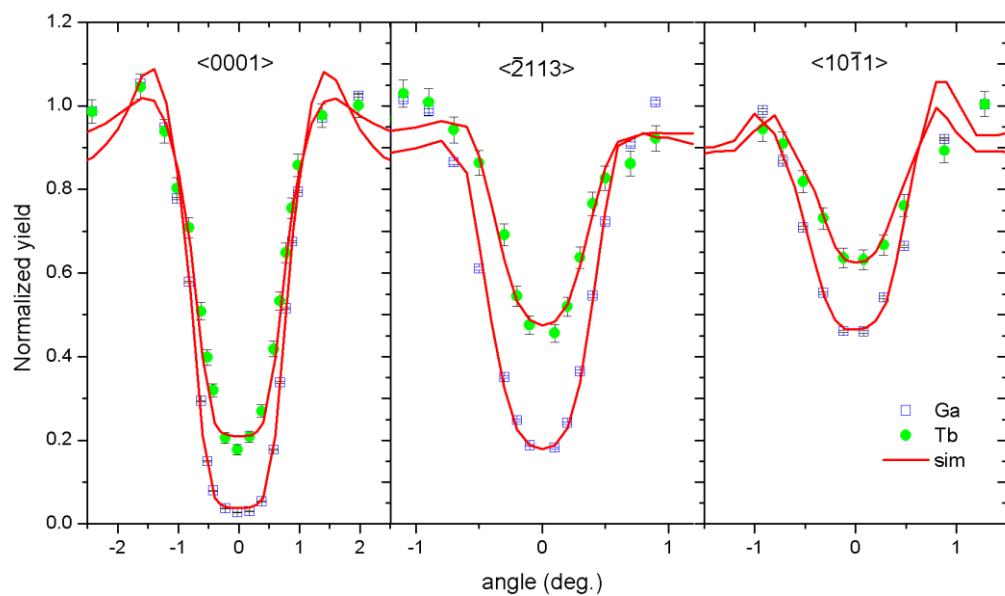


Fig. 11

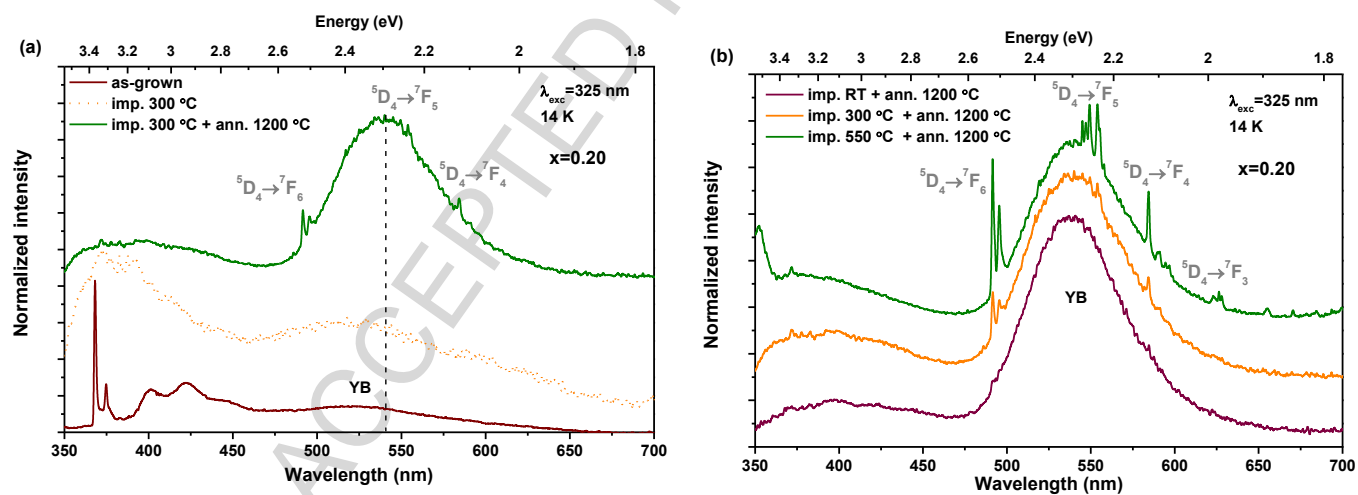


Fig. 12

Highlights

- The impact of implantation temperature on the damage accumulation is investigated.

Rutherford backscattering spectrometry/channeling (RBS/C) measurements show that two damage regions are forming and the damage is not decreasing monotonically with the increase of implantation temperature.

- A good agreement is observed between the damage accumulation obtained from RBS/C and the strain profile derived from symmetric (0002) 2θ - ω X-ray diffraction scans.
- Transmission electron microscopy results show the suppression of basal stacking faults after implantation at 550 °C.
- The optical activity investigated by photoluminescence showed that after thermal annealing, the $^5D_4 \rightarrow ^7F_J$ intra- $4f^8$ transition is detected in all the samples.